Shear modulus imaging by direct visualization of propagating shear waves with phase-sensitive optical coherence tomography

Shaozhen Song
Zhihong Huang
Thu-Mai Nguyen
Emily Y. Wong
Bastien Arnal
Matthew O'Donnell
Ruikang K. Wang

Shear modulus imaging by direct visualization of propagating shear waves with phase-sensitive optical coherence tomography

Shaozhen Song,[a,b] Zhihong Huang,[b] Thu-Mai Nguyen,[a] Emily Y. Wong,[a] Bastien Arnal,[a] Matthew O'Donnell,[a] and Ruikang K. Wang[a,c]

[a]University of Washington, Department of Bioengineering, 3720 15th Avenue NE, Seattle, Washington 98195
[b]University of Dundee, School of Engineering, Physics and Mathematics, Dundee DD1 4HN, Scotland, UK
[c]University of Washington, Department of Ophthalmology, 325 9th Avenue, Seattle, Washington 98104

Abstract. We propose an integrated method combining low-frequency mechanics with optical imaging to map the shear modulus within the biological tissue. Induced shear wave propagating in tissue is tracked in space and time using phase-sensitive optical coherence tomography (PhS-OCT). Local estimates of the shear-wave speed obtained from tracking results can image the local shear modulus. A PhS-OCT system remotely records depth-resolved, dynamic mechanical waves at an equivalent frame rate of ~47 kHz with the high spatial resolution. The proposed method was validated by examining tissue-mimicking phantoms made of agar and light scattering material. Results demonstrate that the shear wave imaging can accurately map the elastic moduli of these phantoms. © *2013 Society of Photo-Optical Instrumentation Engineers (SPIE)* [DOI: 10.1117/1.JBO.18.12.121509]

Keywords: mechanical property; phase-sensitive optical coherence tomography; shear modulus; shear waves; shear-wave velocity; phantom elasticity.

Paper 130385SSRRR received Jun. 3, 2013; revised manuscript received Oct. 15, 2013; accepted for publication Oct. 17, 2013; published online Nov. 8, 2013.

1 Introduction

The elastic properties of tissue are directly related to underlying tissue composition and pathological state. Research has shown that many pathological processes increase the elastic modulus of soft tissue compared to normal.[1] In recent years, a number of image-based tools have been developed to map the elastic properties of soft tissue *in vivo*. The most common approaches leverage the phase-sensitive nature of both ultrasound and magnetic resonance imaging (MRI), linking signal phase directly to displacements. Naturally occurring physiologic processes, such as the heartbeat, or externally applied mechanical forces, induce tissue displacements and deformations as part of the imaging protocol.

Tissue motion has been the subject of research in biomedical imaging for a very long time. Renewed interest in precise tracking using phase-sensitive (PhS) signals began in the late 1980s with the development of "sono-elasticity" methods in which externally driven tissue vibrations were imaged with real-time ultrasound color-flow systems.[2,3] Similar methods based on MRI were developed about a decade later.[4–6] Paralleling these developments, a number of tracking methods emerged to image low frequency or static deformations using both ultrasound and MRI,[5–11] leading to the research field now commonly referred to as "elastography."[12,13] Recently, many of the methods developed over the last two decades in elastography have been applied to radiation-force induced displacements to directly monitor tissue elasticity based on the shear elastic modulus of tissue.[14–16]

Although promising, these methods offer limited spatial resolution to detect small structures and lesions. Optical coherence tomography (OCT)[17–21] is a promising, noninvasive, noncontact technology capable of imaging tissue microstructure at high spatial resolution. It also provides high sensitivity, enabling the detection of submicron scale axial (i.e., along the optical propagation direction) displacements that can be particularly useful for dynamic elastography applications. OCT-based elastography, known as optical coherence elastography (OCE),[17] is a novel extension to OCT to image the mechanical properties of biological tissues on a scale that cannot be achieved with other competing elastography modalities, e.g., ultrasound.[13,22]

Currently, most OCE methods follow an approach similar to that of static elastography. An external load is applied to deform soft tissue and the resulting strain is observed or measured by OCT to derive an elasticity map. Early OCE studies used a static or quasistatic external load,[23,24] with either speckle tracking of the magnitude B-scan or PhS measurements.[25,26,27] The latter provide highly sensitive and highly spatially resolved strain detection.

Dynamic OCE is an active area of research in which acoustic radiation force (ARF)[28,29] and photothermal techniques[30] are used to create an internal dynamic load. Recently, we introduced the use of PhS-OCT to sensitively detect surface acoustic waves propagating on skin[31] and cornea[30] surfaces, leading to quantification of the elasticity of underlying tissues.

Here, we report on the temporal visualization and measurement by PhS-OCT of propagating shear strain waves within tissue-like materials. Such shear waves can probe tissue at greater depths than the surface waves employed in the previous studies. We used a stacked piezoelectric transducer to generate 5 kHz

Address all correspondence to: Ruikang K. Wang, University of Washington, Department of Bioengineering, 3720 15th Avenue NE, Seattle, Washington 98195. Tel: 206 6165025; Fax: 206-685-3300; E-mail: wangrk@uw.edu

shear waves propagating within tissue-mimicking phantoms. They were tracked in space and time using an optimized PhS-OCT system at an equivalent frame rate of 47 kHz. The lateral pixel size is 25 μm, which provides a much higher lateral sampling than in our previous studies, allowing reconstruction of the local shear modulus with a high spatial resolution. The shear-wave velocity was calculated from recorded wave data and the estimated shear modulus (tissue stiffness) was mapped based on a straightforward reconstruction technique. The accuracy of quantitative measurements is verified with a set of experiments on tissue-mimicking phantoms with the controllable stiffness.

2 Materials and Methods

Figure 1 shows a schematic of the system used to generate and detect induced shear waves. It includes (a) a piezoelectric actuator and driving system to generate mechanical waves propagating within the sample and (b) a PhS-OCT system to detect and record mechanical displacements. A PC programmed with LabVIEW (National Instruments, Austin, Texas) controlled the entire system for synchronization and data collection.

2.1 Shear Wave Generation

A low voltage, stacked piezoelectric actuator (Thorlabs, Newton, USA) was used to induce a displacement of 15 μm at a maximum input voltage of 100 V. The external mechanical load is a six-cycle toneburst at 5 kHz. This quasicontinuous wave provides higher signal-to-noise ratio (SNR) for the specified frequency compared to that of a broadband stimulus of the same magnitude. During experiments, the maximum actuator displacement was restricted to 5 μm, with the typical wave amplitude within the specimen <3 μm. With such small strain magnitude, the tissue-like specimen can be considered as linear, thus avoiding the complexity of potential elastic nonlinearities within the soft tissue. A power amplifier (AE Techron, Elkhart, USA) with a controllable voltage gain was used to optimally drive the actuator's capacitance.

A slender stainless steel rod with a small polished tip was fixed to the actuator as the contact to the sample. The tip was in a wedge shape with a width of 1.7 mm, so that the waves generated by this tip can be considered plane waves since this width is much larger than the wavelength. The actuator assembly was then mounted to a precision positioning stage, enabling precise advancement of the actuator-tip to gently contact the specimen at the side (see Fig. 1). The contact between the specimen and the actuator-tip was also visualized in real time by the OCT system (see below), which helped to ensure consistent stimulation conditions for all the measurements.

2.2 Shear Wave Visualization Technique

The PhS-OCT system shown in Fig. 1 detected mechanically induced shear waves. It employs a spectral domain OCT (SD-OCT) setup[32] illuminated by a superluminecent diode (SLD) (DenseLight Semiconductors Ltd., Singapore) emitting a 1310-nm central wavelength with ~46-nm spectral bandwidth. The light from the SLD was coupled to a fiber-based Michelson interferometer via an optical circulator. In the sample arm, light was focused onto the sample, whereas in the reference arm, light was delivered to a stationary mirror. The coupler recombined the backscattered light from both the reference and sample arms to form a spectral interferogram, which was detected by a line-scan camera based spectrometer. A 14 bit, 1024 pixels InGaAs line-scan camera (Sensors Ltd., New Jersey) was used in the spectrometer to produce an A-line rate of 46.992 kHz, corresponding to the sampling rate for mechanical wave capture. This repetition rate is sufficient to fully sample the primary mechanical wave (5 kHz). With the fast processing of spectral interferograms,[33] this system can provide structural and phase map images in real time.[34]

To track shear waves propagating in tissue, the PhS-OCT was operated in M-B-mode, wherein a sequence of 256 A-scans (one M-scan) was captured at every spatial location sequentially within the B-scan (total 128 locations) mode while the actuator repeatedly fired the stimulus. Thus, a complete M-B–scan
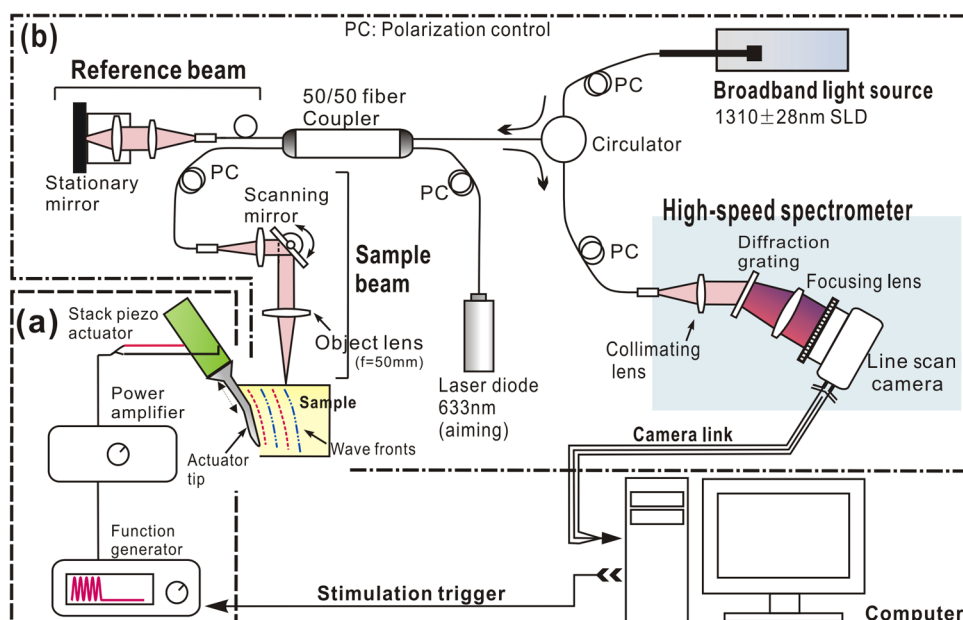
Fig. 1 Schematic of system for shear wave imaging, where (a) sub-system to generate mechanical waves, and (b) PhS-OCT system to detect and record generated shear waves.
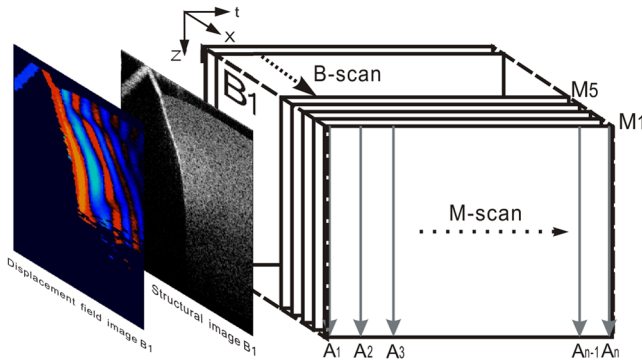
Fig. 2 Illustration of scanning protocol.

consists of 256×128 A-scans. Synchronization of shear wave generation and OCT beam scanning was precisely controlled using custom software written in the LabVIEW language.

PhS data output from the spectral interferograms was used to calculate 256 B-frames of the displacement field. Localized displacement estimates were obtained by comparing phase differences within the M-scan. The axial component of the displacement u_z at a given pixel at time t, i.e., $u_z(x, z, t)$, was computed from the linear relationship between the displacement and the phase difference between adjacent A-scans:[35,36]

$$u_z(x, z, t) = \frac{\Delta\varphi(x, z, t) \cdot \lambda}{4\pi n}, \tag{1}$$

where $\Delta\varphi$ is the detected phase change, λ is the central wavelength of the SLD (1310 nm), and n is the refractive index of the sample. Figure 2 illustrates this scanning approach, where the displacement field over a cross section is imaged with time. A typical structural image is also presented in this figure.

Each M-scan took approximately 15 ms, thus the full M-B-scan took <2 s for a single measurement. The scan range of the B-scan (128 locations) was 2.5 mm, which limited the lateral pixel size to ~25 μm. The axial pixel size is ~5 μm. The dynamic range of the PhS-OCT system was measured to be ~100 dB at 0.5-mm axial depth with a phase noise of 3 mrad. However, the SNR in the region of interest (ROI) of the tissue sample was ~50 dB.

2.3 Tissue-Mimicking Phantoms

Similar to our previous studies,[37] we used tissue-mimicking phantoms to verify our proposed approach. Agar is an easily accessible material that can be used to produce tissue phantoms with controllable mechanical properties similar to those of human soft tissue.[38] By increasing agar concentration, we prepared a series of agar–agar phantoms to mimic Young's modulus (shear modulus) in soft tissue such as within the anterior segment of the eye. To produce these phantoms, the proper amount of agar–agar powder (Fisher Scientific Inc., Pittsburgh, Pennsylvania) was stirred into boiling distilled water until completely dissolved. Before casting into an 8-mm high, 50-mm diameter Petri dish, a few drops of milk were added as scattering particles to facilitate OCT detection. We made the specimens with agar–agar concentrations between 0.5% and 2% (W/V), producing phantoms that could be easily handled mechanically for the studies presented below.

2.4 Shear-Wave Velocity Extraction

After dynamic tissue displacement data $(\vec{u})$ were acquired using the PhS-OCT system, the shear-wave velocity could be reconstructed using a time-of-flight algorithm. In short, shear waves were tracked through time and local displacements along the propagation direction and were correlated with space coordinates at a specific time to estimate shear-wave speed at that time/position.

Shear-wave speed is directly related to the linear elastic modulus of gels and soft tissues in which Poison's ratio approaches 0.5. For these materials, an incompressible elastic model can be assumed in which the shear modulus (μ) is simply proportional to the modulus of linear elasticity, i.e., Young's modulus E, according to the expression $E = 3\mu$. Measurement of either Young's modulus, as in static elastography reconstruction routines, or the shear modulus fully characterizes the linear elastic properties of soft tissue. Consequently, reconstruction of the shear modulus from shear wave measurements can fully characterize the linear elastic properties of the soft tissue sample under study.

In a homogeneous, incompressible, and isotropic medium, the shear-wave speed can be written as

$$C_s = \sqrt{\frac{\mu}{\rho}}, \tag{2}$$

where μ is the shear modulus describing the linear elasticity in the material and ρ is the material density.

For a locally homogenous medium (i.e., spatial variations of elastic properties occur on a larger scale than the shear wavelength), a shear wave at a specified frequency would travel with the constant speed, i.e., the phase delay $\Delta\varphi$ and distance along a wave path Δr is linear; thus,

$$C_s(\omega) = \frac{\omega \Delta r}{\Delta\varphi}. \tag{3}$$

Experimentally, the shear-wave speed can be calculated using the measurements of $\Delta\varphi$ and Δr, i.e., the phase shift and distance that the wave traces at a specific location produce an estimate of the shear-wave speed according to Eq. (3). A number of points along a line can be used to specify the propagation path. The displacement waveforms at these points are then analyzed generating a series of phase delays as a function of corresponding position offsets. Linear fitting to these phase delays produces the shear-wave velocity according to Eq. (3).

2.5 Two-Dimensional (2-D) Reconstruction of Shear Modulus Map

To reconstruct the shear modulus map from shear wave processing, an inverse algorithm is needed. As the localized displacement field $(\vec{u})$ within the sample is captured, not only can the localized wave velocity be extracted at the specified wave path using the method described above, but also the wave velocity map can be reconstructed by solving the wave propagation equation:[39,40]

$$\rho \frac{\partial^2 \vec{u}}{\partial t^2} = \mu \vec{\nabla}^2 \vec{u}. \tag{4}$$

This is a Helmholtz equation assuming that the medium is locally homogeneous and isotropic. Here, μ is the shear modulus

and ρ is the density. By transforming the displacement vector $\vec{u}$ into its three components, Eq. (4) takes the form

$$\frac{\partial^2 u_i}{\partial t^2} = \frac{\mu}{\rho}\left(\frac{\partial^2 u_i}{\partial x^2} + \frac{\partial^2 u_i}{\partial y^2} + \frac{\partial^2 u_i}{\partial z^2}\right), \quad i = (x, y, z). \quad (5)$$

As dynamic wave data obtained from PhS-OCT represent one component of the displacement field along the direction of the probe beam (u_z), two of the three second-order spatial derivatives can be calculated in the imaging area (xz-plane). In our configuration, since the out-of-plane width of the shear wave is far larger than the elevation thickness of the OCT imaging plane, the out-of-plane displacement (u_y) is nearly constant over the slice thickness and variations in this displacement component can be ignored in the ROI; thus

$$\frac{\partial^2 u_z}{\partial y^2} \ll \frac{\partial^2 u_z}{\partial x^2} + \frac{\partial^2 u_z}{\partial x^2}, \quad (6)$$

and Eq. (6) simplifies to

$$\frac{\partial^2 u_z}{\partial t^2} = \frac{\mu}{\rho}\left(\frac{\partial^2 u_z}{\partial x^2} + \frac{\partial^2 u_z}{\partial z^2}\right). \quad (7)$$

Assuming the attenuation of acoustic waves in the frequency range of interest is small, the relationship between shear modulus and shear-wave velocity can be simplified to

$$\mu = \rho V_s^2, \quad (8)$$

where V_s is the shear velocity computed as the square root of the ratio between temporal and spatial second derivatives, which is available from the u_z images estimated in the experiment. Multiplexing these equations, the local shear modulus is then reconstructed as

$$\mu(x, z) = \rho \frac{1}{N} \sum_{n=1}^{N} \frac{\left(\frac{\partial^2 u_z}{\partial t^2}\right)_{x,z}}{\left(\frac{\partial^2 u_z}{\partial x^2} + \frac{\partial^2 u_z}{\partial x^2}\right)_{t=nT}}, \quad (9)$$

where T is the B-frame sampling period and N is the total frame number. The computational power required for this inversion algorithm is much lower than that needed for previous phase-resolved OCE methods.[27] On a standard dual core 3.3 GHz PC, the reconstruction of the 2-D spatial elasticity map from the displacement data took ~5 s.

3 Results

3.1 Quantitative Measurement of Shear Modulus on Tissue-Mimicking Phantoms

Shear wave imaging experiments were performed on a series of tissue-mimicking phantoms with agar–agar concentrations of 0.5%, 0.75%, 1%, 1.5%, and 2% (W/V), respectively. Guided by real-time structural images provided by PhS-OCT, the phantom was advanced by a translation stage so that the actuator-tip was mechanically coupled to the phantom surface at the side (see Fig. 1). One typical image of the displacement field, overlaid onto the structural image of the phantom, is presented in Fig. 3.
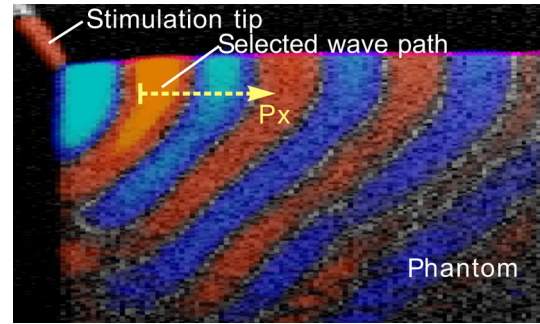
Fig. 3 Displacement field overlaid onto structural image of a homogenous phantom.

With the stimulation source generating a 5 kHz mechanical wave, shear wave phase images from the different agar–agar phantoms showed wave patterns of varying wavelength. Typical patterns from four phantoms are shown in Fig. 4. Differences in the wavelength are clearly distinguishable between each specimen, demonstrating differences in wave velocities, thus the stiffness. We note that because the free boundaries are very close to the shear wave source, induced mechanical waves are most likely Rayleigh-like with the mixed longitudinal and shear components. For this geometry, the estimated propagation speed is closer to that of Rayleigh waves. As Rayleigh waves exhibit slower propagation speeds than the bulk shear waves, the simple analysis presented above for bulk shear waves likely underestimates the shear-wave speed by about 5%. However, this estimate can be used to compare relative values of shear modulus between different materials.

To calculate the shear-wave velocity in the phantom with the time-of-flight method, a wave propagation path with a known direction needs to be defined. The target shear wave paths are selected near the sample surface and about one wave length in depth, where the wave propagation direction is nearly horizontal. For every pixel on this wave path, temporal displacement data are taken for analysis. As an example, wave traces on the path shown in Fig. 3 are plotted in Fig. 4(e). By calculating the phases at 5 kHz frequency for each wave trace, the phase delay versus offset distance from the first point is shown in Fig. 4(f). The slope, $\Delta r/\Delta\varphi$, resulting from linear fitting, is then used to solve Eq. (3) for the wave velocity C_s. Figure 5 shows the reconstructed shear modulus map for an agar phantom with 0.5% agar concentration. The shear modulus map (color scale) is superimposed on the B-scan (gray scale). The shear modulus is displayed wherever the correlation coefficient of the linear fitting is greater than 0.99. The median shear-wave speed across the imaging plane is estimated to be 1.8 ± 0.5 m/s, corresponding to a shear modulus of 3.28 ± 1.77 kPa.

In Fig. 6 measured shear wave velocities in agar–agar phantoms are presented, along with the results extracted from prior literature.[38] Note that the prior method used magnetic resonance elastography to estimate shear-wave speed at an excitation frequency of 400 Hz for the results presented in Fig. 6. We performed repeated measurements on each specimen ($n = 5$) to provide an estimate of standard deviations (SDs), as shown by the error bars in this figure.

The measured shear wave velocities generally agreed well with the literature values: the deviation is smaller than 6% of the shear-wave speed for the different agar concentrations. This value is comparable to the SD of the experimental measurements, which is ~5% of the shear-wave speed. The consistent
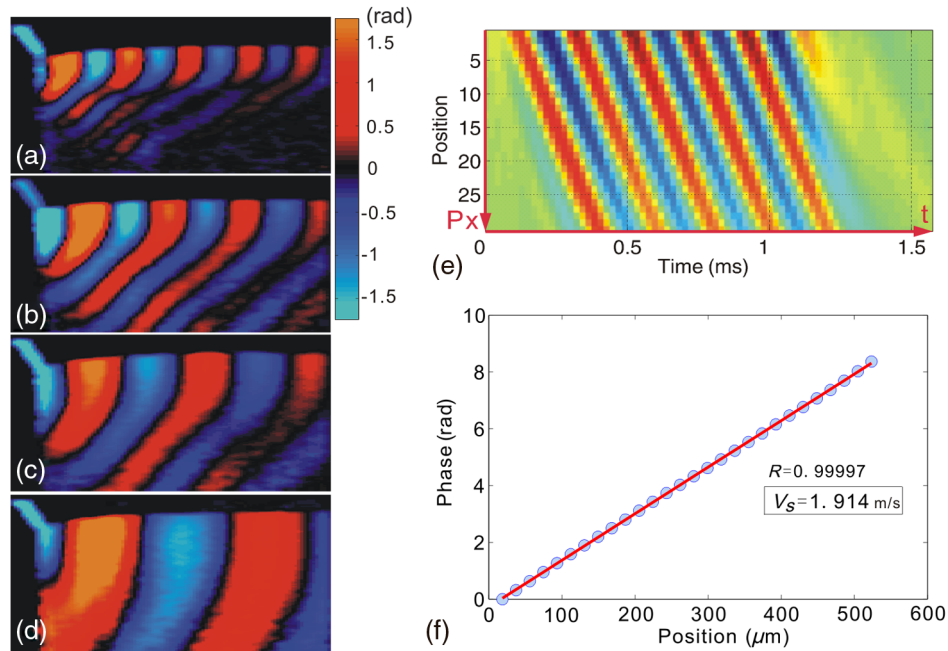
Fig. 4 (a–d) Wave propagation pattern in agar phantoms with agar concentration: (a) 0.5%, (b) 0.75, (c) 1%, and (d) 2%, respectively [see also (Videos 1–4, MPEG, 4.7 MB each) [URLs: http://dx.doi.org/10.1117/1.JBO.18.12.121509.1, http://dx.doi.org/10.1117/1.JBO.18.12.121509.2, http://dx.doi.org/10.1117/1.JBO.18.12.121509.3, http://dx.doi.org/10.1117/1.JBO.18.12.121509.4], corresponding to (a–d)]. (e) Wave traces along the specified wave propagation path shown in Fig. 3 as "Px." (f) Linear fitting of the phase delays versus position offsets from the first point.
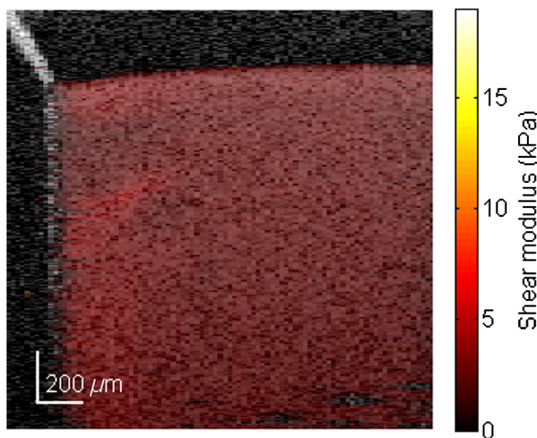
Fig. 5 Shear modulus map of a 0.5% agar phantom.
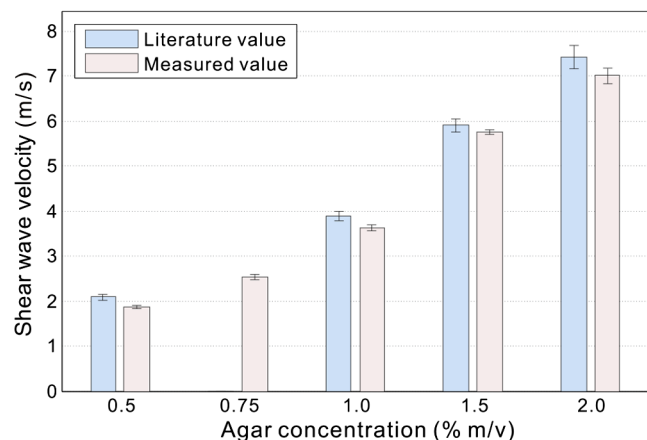
Fig. 6 Measurement results of shear-wave velocity in agar phantom.

underestimation can also be a result of measuring the velocity within about one wavelength of a free surface where Rayleigh wave effects tend to reduce the apparent wave velocity. In any event, the results presented in Fig. 6 are very precise (i.e., small measurement errors) and match well with the literature values for shear-wave speed in similar agar gels.

3.2 2-D Shear Modulus Reconstruction for Phantom with Inclusion

In Fig. 7(e), the structural image of an agar phantom with a cylindrical inclusion is presented. The inclusion was ∼500 µm in diameter and made of 1% agar solution, while the background was made of 0.5% agar. In the B-mode OCT image [Fig. 7(e)], the boundary of the hard inclusion is barely visible, as indicated by the dotted line. However, the stimulation tip attached to the left side of the tissue-mimicking phantom is clearly visible.

After processing M-B-scan data, the B-frame sequence of displacement maps was generated, i.e., full wave propagation data. Typical phase frames are presented in Figs. 7(a)–7(d) at different time points, where propagation of shear waves can be observed.

A major benefit of directly visualizing these wave patterns is that the wave propagation direction at specific locations can be easily identified as normal to the displacement front. This facilitates the extraction of shear-wave velocity using the time-of-flight method. Two propagation paths were selected, as shown in Fig. 7(e), each containing 20 wave traces. For each path, we performed the time-of-flight method to estimate the wave velocity, as shown in Fig. 7(g). The shear-wave velocity was calculated by linear fitting to these curves, yielding 1.71 and 4.13 m/s in paths 1 and 2 [Fig. 7(e)], respectively. These results are in good agreement with the wave speeds found in equivalent gels (cf. Fig. 6). By substituting these values in Eq. (2), the shear
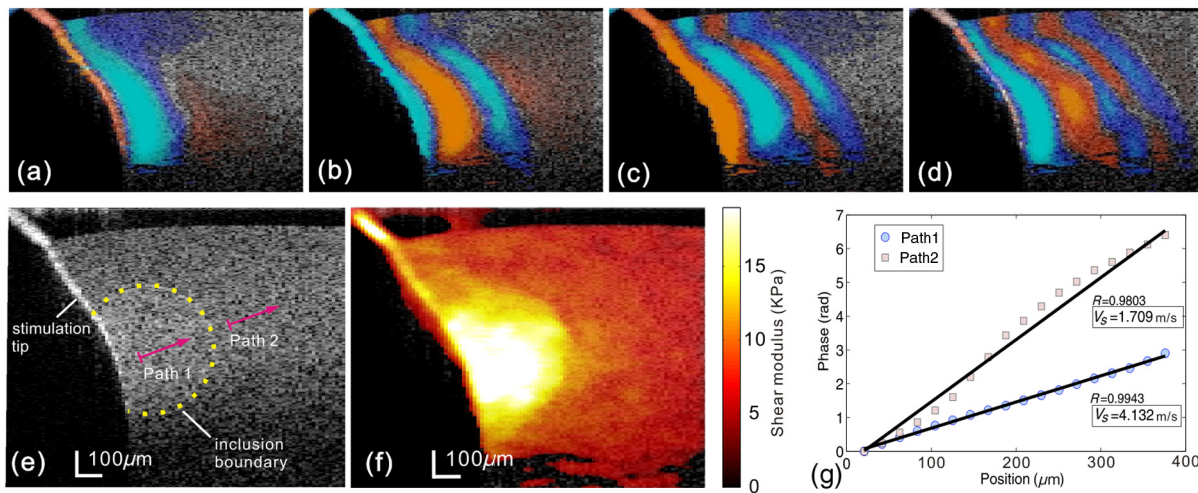
Fig. 7 (a–d) Displacement field B-frame images at different time points [see also (Video 5, MPEG, 3.5 MB) [URL: http://dx.doi.org/10.1117/1.JBO.18.12 .121509.5]: (a) $t = 2$ Ts (b) $t = 4$ Ts (c) $t = 6$ Ts (d) $t = 8$ Ts, respectively. (e) B-mode structural image of agar phantom with inclusion. (f) Quantitative map of shear modulus (μ) computed from the dynamic shear wave visualization. (g) Linear fitting of phase delays versus position offsets for two selected wave propagation paths.

moduli in these two regions are 2.92 and 17.06 kPa, respectively. Note that these two paths are located, respectively, in the hard inclusion and soft background.

To obtain a quantitative shear modulus map in the measured phantom, we applied the reconstruction algorithm to all spatial–temporal wave propagation data. The result is shown in Fig. 7(f) with the shear modulus color-coded and overlaid onto the gray scale structural image using precisely the same display dynamic range as that of Fig. 5. In the region near the contact with the stimulation tip, the shear modulus value is not accurate because the simple wave equation of Eq. (7) is not applicable in the immediate source region. Overall, this image clearly demonstrates the capability of the current approach to differentiate stiffness within mechanically heterogeneous tissue. The position and shape of the inclusion are clearly visible, with the boundary-matched well with its expected location. The lateral resolution of the shear modulus map is affected by two main factors. First, the linear fitting of the phase delay curve is performed over $\sim 500~\mu m$. Second, the shear wave can be diffracted by the inclusion. By comparing shear modulus values with the time-of-flight method, consistency is maintained in both the stiff lesion region (~ 17 kPa) and the homogenous background (~ 3 kPa).

4 Discussion and Conclusions

In this study, we demonstrated a novel shear wave imaging technique combining acoustic biomechanical analysis and remote PhS-OCT measurement of dynamic displacement fields. Using the time-of-flight method, i.e., analyzing phase delays versus distance traveled by the dynamic wave, the shear-wave velocity in the specimen can be calculated to provide quantification of the shear modulus. Through simple algebraic inversion of the wave equation, we have shown that tissue elasticity can be successfully mapped.

Shear wave imaging offers a new way to measure the localized shear modulus, while PhS-OCT provides a complementary structural image of the same tissue. The ability to measure the localized shear modulus in conjunction with the morphology at high resolution has significant advantages over conventional ultrasound or MRI methods for those applications where OCT represents an appropriate imaging modality. Indeed, we hope

that this approach will lay the foundation for future *in vivo* studies of the mechanical properties of tissue microstructures, especially for clinical applications in ophthalmology (cornea and intraocular lens) and dermatology (epidermis and dermis).

The model used here for image reconstruction assumed a constant propagation speed as a function of frequency with no propagation loss resulting from viscosity. Of course, both of these assumptions are not accurate for shear wave propagation in soft tissue over the kilohertz range. Both velocity dispersion and frequency dependent attenuation are significant. Future studies will explore frequency dependent propagation effects and attempt to capture dispersion measurements as part of the shear wave imaging protocol.

Although elastic modulus maps in these well-controlled phantoms were well correlated with the physical characteristics of the gels used, there were systematic variations in reconstructed values due to the limitations in the assumed wave propagation model. For example, an infinite medium is assumed, in which there are no reflected waves.[41] By definition, elastic heterogeneities produce reflected waves which are not captured in the simple model of Eqs. (4)–(9). Also, diffraction from a finite source has not been modeled. Future studies will look at ways to capture these physical effects into a more sophisticated propagation model leading to more robust reconstructions in highly heterogeneous tissue. Biological tissue can exhibit such a complex, highly heterogeneous, structure. A first-order approximation considers different tissue types as effective media with an effective shear modulus that reflects both the background and elastic heterogeneities smaller than the shear wavelength. The simple reconstruction method presented here is very powerful and should be the starting point for any future improvements.

Tissue motion due to physiologic effects not correlated with the induced displacements can limit the effectiveness of any dynamic elastography system. Many techniques have been proposed to minimize the influence of motion artifacts on dynamic displacement measurements.[42] Given the high temporal sampling rate of the shear wave imaging system presented here, motion compensation algorithms should be possible. Future studies will also be directed toward robust algorithms

minimizing the effects of potential motion artifacts on images of the shear-wave velocity.

Finally, there are additional limitations on the method presented here due to the direct contact required to launch shear waves. Given the high sensitivity of the PhS-OCT detection system, shear wave generation using a nondestructive radiation source may be a feasible approach to noncontact implementation. Both focused UV radiation serving as a photoacoustic source, as well as focused ultrasound acting as an ARF, will be tested as tools to induce propagating shear waves. This will extend the possibility of a noncontact shear wave imaging elastography with our method. It is hoped that the developments reported here will help to improve this novel elastography diagnostic technique for widespread biomedical applications.

Acknowledgements

References

1. Y. C. Fung, *Biomechanics: Mechanical Properties of Living Tissues*, 2nd ed., Springer, Berlin (1993).
2. T. A. Krouskop, D. R. Dougherty, and F. S. Vinson, "A pulsed Doppler ultrasonic system for making noninvasive measurements of the mechanical properties of soft tissue," *J. Rehabil. Res. Dev.* **24**(2), 1–8 (1987).
3. R. M. Lerner et al., "Sono-elasticity: medical elasticity images derived from ultrasound signals in mechanically vibrated targets," *Acoust. Imaging* **16**, 317–327 (1989).
4. R. Muthupillai and R. L. Ehman, "Magnetic resonance elastography," *Nat. Med.* **2**(5), 601–603 (1996).
5. L. Axel and L. Dougherty, "Heart wall motion: improved method of spatial modulation of magnetization for MR imaging," *Radiology* **172**(2), 349–350 (1989).
6. E. A. Zerhouni et al., "Human heart: tagging with MR imaging—a method for noninvasive assessment of myocardial motion," *Radiology* **169**(1), 59–63 (1988).
7. M. Tristam et al., "Application of Fourier analysis to clinical study of patterns of tissue movement," *Ultrasound Med. Biol.* **14**(8), 695–707 (1988).
8. M. Bertrand et al., "Ultrasonic biomechanical strain gauge based on speckle tracking," in *IEEE Ultrasonics Symposium*, Montreal, Que, pp. 859–863 (1989).
9. J. Meunier and M. Bertrand, "Ultrasonic speckle motion inherent to tissue motion: theory and simulation," in *IEEE Ultrasonics Symposium*, Montreal, Que, pp. 865–868 (1989).
10. M. O'Donnell, A. R. Skovoroda, and B. M. Shapo, "Measurement of arterial wall motion using Fourier based speckle tracking algorithms." in *IEEE Ultrasonic Symposium*, pp. 1101–1104 (1991).
11. M. O'Donnell et al., "Internal displacement and strain imaging using ultrasonic speckle tracking," *IEEE Trans. Ultrasonics Ferroelectr. Freq. Control* **41**(3), 314–325 (1994).
12. J. Ophir et al., "Elastography: ultrasonic imaging of tissue strain and elastic modulus *in vivo*," *Eur. J. Ultrasound* **3**(1), 49–70 (1996).
13. J. Ophir et al., "Elastography: imaging the elastic properties of soft tissues with ultrasound," *J. Med. Ultrasound* **29**, 155–171 (2002).
14. A. P. Sarvazyan et al., "Shear wave elasticity imaging: a new ultrasonic technology of medical diagnosis," *Ultrasound Med. Biol.* **24**(9), 1419–1435 (1998).
15. K. R. Nightingale et al., "On the feasibility of remote palpation using acoustic radiation force," *J. Acoust. Soc. Am.* **110**(1), 625–634 (2001).
16. J. Bercoff, M. Tanter, and M. Fink, "Supersonic shear imaging: a new technique for soft tissue elasticity mapping," *IEEE Trans. Ultrasonics Ferroelectr. Freq. Control* **51**(4), 396–409 (2004).
17. C. Sun, B. Standish, and V. X. D. Yang, "Optical coherence elastography: current status and future applications," *J. Biomed. Opt.* **16**(4), 043001 (2011).
18. A. F. Fercher et al., "Optical coherence tomography—principles and applications," *Rep. Prog. Phys.* **66**, 239–303 (2003).
19. P. H. Tomlins and R. K. Wang, "Theory, developments and applications of optical coherence tomography," *J. Phys. D* **38**(15), 2519–2535 (2005).
20. R. K. Manapuram et al., "*In vivo* estimation of elastic wave parameters using phase-stabilized swept source optical coherence elastography," *J. Biomed. Opt.* **17**(10), 100501 (2012).
21. B. F. Kennedy et al., "*In vivo* dynamic optical coherence elastography using a ring actuator," *Opt. Express* **17**(24), 21762–2172 (2009).
22. S. H. Cho et al., "Acoustic radiation force impulse elastography for the evaluation of focal solid hepatic lesions: preliminary findings," *Ultrasound Med. Biol.* **36**(2), 202–208 (2010).
23. J. Rogowska et al., "Optical coherence tomographic elastography technique for measuring deformation and strain of atherosclerotic tissues," *Heart* **90**(5), 556–562 (2004).
24. H.-J. Ko et al., "Optical coherence elastography of engineered and developing tissue," *Tissue Eng.* **12**(1), 63–73 (2006).
25. K. M. Kennedy et al., "Needle optical coherence elastography for tissue boundary detection.," *Opt. Lett.* **37**(12), 2310–2312 (2012).
26. B. F. Kennedy et al., "Strain estimation in phase-sensitive optical coherence elastography," *Biomed. Opt. Express* **3**(8), 1865–1879 (2012).
27. X. Liang et al., "Optical micro-scale mapping of dynamic biomechanical tissue properties," *Opt. Express* **16**(15), 11052–11065 (2008).
28. X. Liang et al., "Acoustomotive optical coherence elastography for measuring material mechanical properties," *Opt. Lett.* **34**(19), 2894–2896 (2009).
29. M. Razani et al., "Feasibility of optical coherence elastography measurements of shear wave propagation in homogeneous tissue equivalent phantoms," *Biomed. Opt. Express* **3**(5), 972–980 (2012).
30. C. Li et al., "Noncontact all-optical measurement of corneal elasticity," *Opt. Lett.* **37**(10), 1625–1627 (2012).
31. C. Li et al., "Determining elastic properties of skin by measuring surface waves from an impulse mechanical stimulus using phase-sensitive optical coherence tomography," *J. R. Soc., Interface* **9**(70), 831–841 (2012).
32. R. K. Wang and A. L. Nuttall, "Phase-sensitive optical coherence tomography imaging of the tissue motion within the organ of Corti at a subnanometer scale: a preliminary study," *J. Biomed. Opt.* **15**(5), 056005 (2010).
33. R. K. Wang and L. An, "Doppler optical micro-angiography for volumetric imaging of vascular perfusion *in vivo*," *Opt. Express* **17**(11), 8926–8940 (2009).
34. R. K. Wang and Z. Ma, "A practical approach to eliminate autocorrelation artefacts for volume-rate spectral domain optical coherence tomography," *Physi. Med. Biol.* **51**(12), 3231–3239 (2006).
35. R. K. Wang, Z. Ma, and S. J. Kirkpatrick, "Tissue Doppler optical coherence elastography for real time strain rate and strain mapping of soft tissue," *Appl. Phys. Lett.* **89**(14), 144103 (2006).
36. R. K. Wang, S. Kirkpatrick, and M. Hinds, "Phase-sensitive optical coherence elastography for mapping tissue microstrains in real time," *Appl. Phys. Lett.* **90**(16), 164105 (2007).
37. C. Li et al., "Evaluating elastic properties of heterogeneous soft tissue by surface acoustic waves detected by phase-sensitive optical coherence tomography," *J. Biomed. Opt.* **17**(5), 057002 (2012).
38. U. Hamhaber et al., "Comparison of quantitative shear wave MR-elastography with mechanical compression tests," *Magn. Reson. Med.* **49**(1), 71–77 (2003).
39. J. Ophir et al., "Elastography a quantitative method for imaging the elasticity of biological tissues," *Ultrasonic Imaging* **13**(2), 111–134 (1991).
40. J. Achenbach, *Wave Propagation in Elastic Solids*, Elsevier, Amsterdam, North Holland (1975).
41. Y. Yamakoshi, J. Sato, and T. Sato, "Ultrasonic imaging of internal vibration of soft tissue under forced vibration," *IEEE Trans. Ultrasonics Ferroelectr. Freq. Control* **37**(2), 45–53 (1990).
42. B. J. Fahey, S. J. Hsu, and G. E. Trahey, "A novel motion compensation algorithm for acoustic radiation force elastography," *IEEE Trans. Ultrasonics Ferroelectr. Freq. Control* **55**(5), 1095–1111 (2008).